High capacity Mn-Fe-Mo/FSM-16 sorbents in hot coal gas desulfurization and mechanism of elemental sulfur formation

Hong Xia [a], Bingsi Liu [a,*], Qian Li [b], Zhaobiao Huang [a], Allan Shi-Chung Cheung [b,*]

[a] Department of Chemistry, School of Science, Tianjin University and Collaborative Innovation Center of Chemical Science and Engineering (Tianjin), Tianjin 300072, China
[b] Department of Chemistry, University of Hong Kong, Pokfulam Road, Hong Kong, China

ABSTRACT

A series of newly developed Mo incorporated Mn-Fe supported on cost-effective mesoporous silica for the reactive adsorption desulfurization process is reported. The performance of the new sorbents was evaluated at 550–750 °C over a fixed-bed reactor. 50% 4Mn1Fe-3%Mo/FSM-16 exhibited better desulfurization performance at 600 °C with a breakthrough sulfur capacity (BSC) of 18.15 g S/100 g sorbent compared to 50% 4Mn1Fe/FSM-16 sorbent. High sulfur capacity (90% of the initial sulfur capacity) of sorbent was maintained after multiple sulfidation-regeneration cycles, which revealed 50% 4Mn1Fe-3%Mo/FSM-16 possessed strong durability. A large amount of elemental sulfur was produced instead of sulfur dioxide (SO_2) by a simple regeneration. Moreover, the mechanism of sulfidation-regeneration was confirmed in situ using highly sensitive time-of-flight mass-spectrometry (TOF-MS) for the first time.

© 2016 Elsevier B.V. All rights reserved.

1. Introduction

In recent years, the environmental problem and energy crisis are becoming increasingly acute with economic development. Coal is the most abundant fossil fuel with relatively low price. However, a large amount of pollutants are released during the combustion of coal, which is well known to have detrimental impacts on human health and our environment. Recently, huge efforts have been put to capture CO_2, SO_x and NO_x [1,2] from the environment. Due to environmental concerns in using fossil fuels, one of the current trends in energy issues is to improve technology, especially, the integrated gasification combined cycle (IGCC)[3–5]. In an IGCC system, sulfur removal is a critical process, which minimizes equipment corrosion and the emission of air contaminants, therefore, various technologies have been developed for improving the desulfurization process to meet different requirements[6]. From environmental points of view and also thermal efficiency, hot coal gas desulfurization (HGD) process is attractive, which avoids the heat exchange and enhances the process efficiency [7,8].

In high-temperature desulfurization process, because of the high temperature condition, only transition metal oxides based solid sorbents are suitable choice. Westmoreland and Harrison[9] pointed out that the metal oxides of zinc, ferric, manganese, molybdenum, vanadium, calcium, strontium, barium, cobalt, copper and tungsten have thermodynamic feasibility, especially, the sorbents containing zinc, ferric, copper, manganese, calcium and rare earth elements have been extensively reported for hot coal gas desulfurization[10–16]. Although zinc oxide is recognized as highly effective sorbent in conventional desulfurization process, its performance is limited by thermal instability due to chemical or mechanical degradation at high temperature under reducing atmosphere. However, Mn-based sorbents have attracted wide research interests in recent years because of their large sulfur capacity, high mechanical stability and fast initial reaction rate for the removal of H_2S in the range of 400–1000 °C [17]. The potential of Mn-based sorbents is often improved by the addition of other metals, such as copper, zinc and ferric [18,19]. Unfortunately, the applications of zinc and copper oxides are limited due to zinc evaporation and the reduction of copper oxides in reducing atmosphere. Moreover, low desulfurization efficiency and high cost are also the drawbacks in using copper oxides. When all things are considered, iron oxide is more promising than others due to its good desulfurization performance, low cost and abundant raw materials such as iron ore and red mud [13,20]. A combination of manganese oxides and ferric oxides improves the desulfurization efficiency (or precision) of the former and the mechanical strength of the latter[21], which also removes H_2S and

COS simultaneously. In addition, molybdenum has been reported to be one of the candidates for desulfurization[22]. Zhang et al. [23] reported that the addition of molybdenum to Mn-based sorbents could improve the sulfur capacity. Wang et al. [24] claimed that molybdenum was able to effectively increase the desulfurization efficiency of Fe-based sorbents. However, further improvement of desulfurization performance of metal oxides alone or composite metal oxides becomes challenging because of limitations in diffusion resistance, mechanical strength and sintering. In order to overcome these obstacles, a combination of mesoporous materials with high surface area, large pore volume and tunable pore structure with metal oxides has been considered as a powerful strategy, which gains researchers' attentions rapidly. A series of sorbents supported on mesoporous silica including MCM-48, SBA-15 and KIT-6, has been prepared and evaluated [18,25–27]. But these advanced support materials are not cost-effective, whose synthesis are generally performed using relatively expensive silica precursor tetraethoxysilane (TEOS) or template [(polyethylene oxide)$_{20}$-(polypropylene oxide)$_{70}$-polyethylene oxide)$_{20}$-Pluronic P123]. Thus, high cost of mesoporous materials limits their large-scale industrial applications.

Another important factor to be taken into account for industrial desulfurization is the regeneration product, which affects directly the complexity of desulfurization procedure. In most cases, sulfur dioxide (SO_2) is inevitably the product during the regeneration of sorbents, which requires further cleaning up treatment. Comparing with SO_2, elemental sulfur is the most ideal regeneration product, which not only simplifies the desulfurization procedure, it also has a market value. In addition, sulfur is easily stored and can be transported safely. Addressing these concerns, we report, in this work, a new developed family of high-efficiency Mn-Fe-Mo sorbents supported on cost-effective mesoporous silica. The support (FSM-16) is synthesized from economical and easily available fumed silica and no hydrothermal treatment is required, which could significantly simplify the scale-up problems in synthetic procedure. The addition of Mo to Mn-Fe based sorbents results in an improvement in sulfur capacity due to high dispersion and electronic effects. It is noteworthy that elemental sulfur instead of SO_2 was obtained during the sulfidation/regeneration process, avoiding the expensive and complex claus process. It is surprising that there are only very limited reports about in situ studies on the mechanism of sulfidation/regeneration over Mn-based sorbents particularly for the formation of elemental sulfur. With this motivation, the highly sensitive time-of-flight mass-spectrometry (TOF-MS) has been employed to investigate the hot gas desulfurization process in detail. In view of low cost and good sulfidation/regeneration performance, the newly developed sorbents should be very useful in industrial applications.

2. Experimental

2.1. Support synthesis

FSM-16 was synthesized using the method reported by Inagaki et al. [28]. 12.0 g fumed silica and 8.0 g NaOH were dissolved in 120 mL deionized water (DW) and the mixture was stirred at ambient temperature (AT) for 3 h followed by drying at 100 °C. The dried solid was calcined at 700 °C and immersed in water to obtain kanemite paste (δ-Na$_2$Si$_2$O$_5$). All of the kanemite paste was dispersed in 300 mL of an aqueous solution of cetyltrimethylammonium bromide (0.1 mol L^{-1}) and heated at 70 °C for 3 h with stirring. Subsequently, the pH value was adjusted carefully to 8.5 with diluted HCl (2 mol L^{-1}) and the suspension was left at 70 °C for another 3 h with stirring. The resulting product was filtered,

washed with water repeatedly, dried in air and calcined at 550 °C for 6 h.

2.2. Sorbents preparation

A series of aMn-bFe-xMo/FSM-16, where a/b is the molar ratio of Mn/Fe and x is the loading of Mo, was prepared via sol-gel method [14,23,25]. Taking the preparation of 50% 4Mn1Fe-3%Mo/FSM-16 as an example, 2.972 g of Mn(NO$_3$)$_2$ aqueous solution, 0.848 g of Fe(NO$_3$)$_3$·9H$_2$O and 0.058 g of (NH$_4$)$_6$Mo$_7$O$_{24}$·4H$_2$O were added to 25 mL DW. After the addition of 3.414 g citric acid, 0.8 g FSM-16 was added. The sol was continuously stirred at 60 °C until a viscous gel was formed. The gel was aged at AT for 3 days and finally calcined at 550 °C for 6 h. All samples were based on 4:1 molar ratio of Mn: Fe according to our previous report, which presented the largest amount of (Fe$_x$Mn$_{2-x}$)O$_3$ solid solution and showed the best desulfurization performance[21]. x was set as 3%, 5%, 10% and 25%. The loading of the active metal oxides for all samples was 50 wt%.

2.3. Performance assessments

Evaluations of sorbents for sulfidation and regeneration were conducted in a fixed-bed quartz reactor with an inner diameter of 10 mm at atmospheric pressure in the range of 550–700 °C using simulated hot coal gas with or without steam (0.33% H$_2$S, 10.5% H$_2$, 18% CO and N$_2$ balance). The experimental setup is shown in Scheme 1. In each experiment, 0.5 g sorbent was packed into the reactor and the reaction temperature was controlled by a K-type thermocouple. The sorbents were first heated to the desired temperature in nitrogen atmosphere at a rate of 10 °C/min and subsequently, the gas mixture was passed through the reactor at a steady weight hourly space velocity (WHSV) of 9×10^3 mL h^{-1}g^{-1} using a mass flow controller (D07-7B/ZM, Beijing Seven-star Electronics Co., Ltd, China) for desulfurization. The concentration of H$_2$S in the inlet/outlet gas was analyzed by the method of iodometric titration.

The breakthrough curve is expressed as the amount of outlet concentration of H$_2$S versus time. The amount of sulfur captured by the sorbent at the breakthrough point (the sulfur content in the outlet lower than 50 mg/m^3) was defined as the breakthrough sulfur capacity (BSC), which was used to evaluate the performance of sorbents. It was calculated by following formula:

$$SC \left(\frac{g\ of\ sulfur}{100\ g\ of\ sorbent} \right) = WHSV \times \frac{M_S}{V_m} \times \frac{22.4}{M_{H_2S}} \left[\int_0^t (C_{in} - C_{out})\,dt \right] \times 10^{-4} (1)$$

Where SC is the effective sulfur capacity of sorbent (g sulfur/100 g sorbent); WHSV is the weight hourly space velocity (L h^{-1} g^{-1}); M_s and M_{H2S} are the molar weight of S (32.06 g mol^{-1}) and H$_2$S (34.06 g mol^{-1}), respectively; V_m is the molar volume of H$_2$S at 1 atm and 25 °C (24.5 L mol^{-1}); t is the reaction time for desulfurization (h), and C_{in} and C_{out} are the inlet and outlet concentration of H$_2$S (mg/m^3).

After sulfidation, the used sorbent was heated to 700 °C at 10 °C/min with a N$_2$ flow of 150 mL/min which corresponded to a WHSV value of 9000 mL h^{-1} g^{-1}. Then 5 vol% O$_2$/N$_2$ mixtures were switched to regenerate the sulfidation sorbent at 700 °C. SO$_2$ in outlet was detected using a KMnO$_4$ solution (Scheme 1c). Elemental sulfur formed during regeneration was condensed at the outlet of the reactor. When no sulfur element was formed or SO$_2$ in the effluent could not be detected, the regeneration was stopped. The regenerated sample was directly used for sulfidation test in the next cycle.
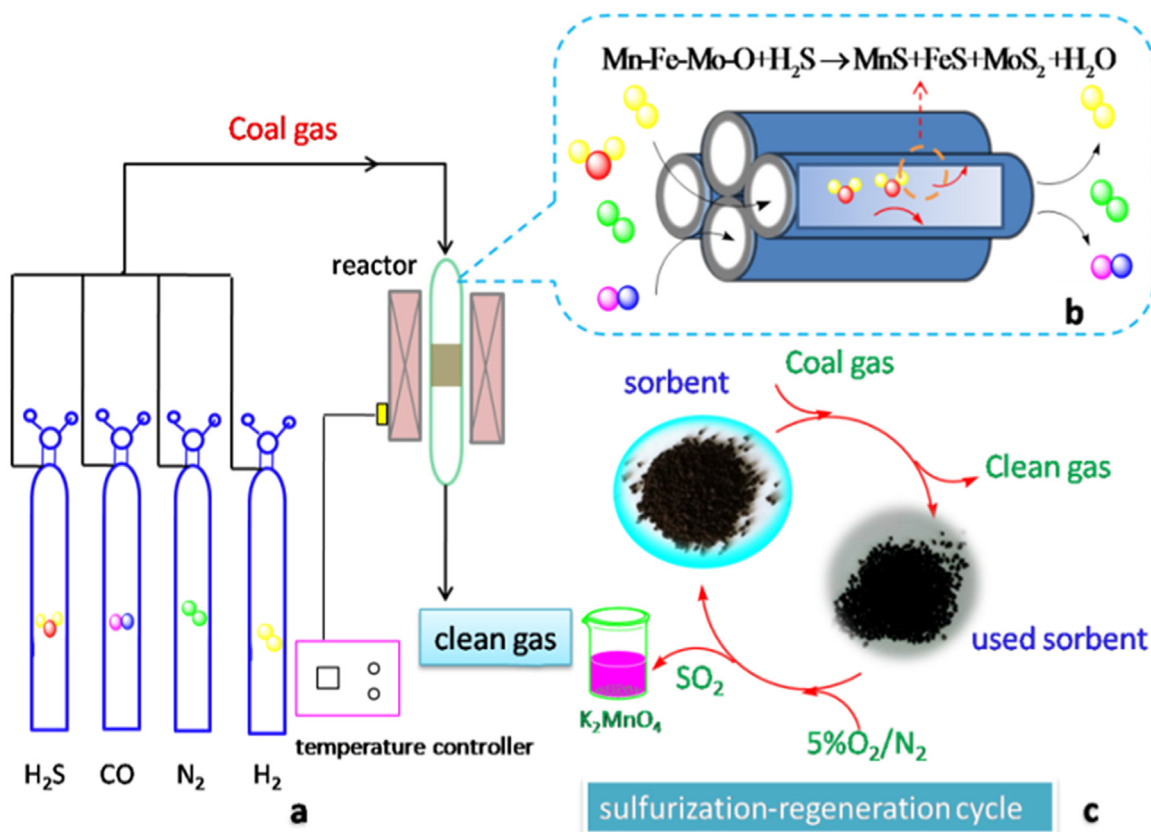
Scheme 1. Schematic diagram of sulfidation/regeneration test (a) experimental setup; (b) simple model for stable 50% 4Mn1Fe-*x*Mo/FSM-16 for hot coal gas desulfurization; (c) sulfidation/regeneration cycle.

2.4. Characterization techniques

The wide-angle X-ray diffraction (XRD) patterns were conducted over a PANalytical automatic diffractometer using Ni filtered Cu Kα radiation (λ = 0.15406 nm) at settings of 40 kV and 50 mA. The small-angle XRD was recorded with a Rigaku automatic diffractometer equipped with a Ni filtered Cu K_a radiation source (20 kV, 30 mA). Nitrogen adsorption isotherms of the sorbents were measured using a domestic adsorption system at 77 K [29]. The pore size distribution curves were analyzed with the adsorption branch by Barrett, Joyner & Halenda (BJH) method.

The structures and morphology of sorbents were investigated by high-resolution transmission electron microscopy (HRTEM) on a Tecnai G2F20 electron microscope at 200 kV accelerating voltage. The compositions of sorbents were analyzed by the energy dispersive X-ray (EDX) technique. Fourier transform infrared absorption spectroscopy (FT-IR) was performed with a BIO-RAD FTS 3000 spectrophotometer with the sample on a KBr wafer. The UV–vis diffuse reflectance spectroscopy (UV-DRS) was recorded on a Shimadzu UV-2101 spectrophotometer in the wavelength range of 200–800 nm by using FSM-16 as reference. Absorbance was converted to F(R) according to the Kubelk-Munk function (A = −lg(R), F(R) = (1-R)^2/2R). Temperature-programmed reduction (TPR) was conducted in a domestic system using gas chromatography (GC) with thermal conductivity detector (TCD) for monitoring hydrogen consumption. The typical operation was described in our report previously [23].

2.5. In situ TOF-MS analysis

The mechanism of sulfidation/regeneration was investigated by analyzing the species from thermal desorption over 50% aMn-bFe-*x*Mo/FSM-16 sorbents using TOF-MS. The TOF-MS setup was described in detail elsewhere [30,31]. Typically, approximately 50 mg sorbent was placed between two quartz-wool plugs inside a quartz reactor (*i.d.* 4 mm). The thermal desorption temperature was monitored by a thermocouple. The species in the gas effluent after passing through the sorbent were ionized by an ArF excimer laser; the ionized species were accelerated by an assembly of acceleration plates, focused by Einzellens and drifted through a typical TOF field-free region before reaching the microchannel plate (MCP) detector. Signals from the detector were collected and analyzed by a 300 MHz digital storage oscilloscope. After the thermal desorption process, the sample was flushed only with pure argon until a stable base line was obtained (700 °C). The sample was then regenerated with 6 vol% $^{18}O_2$/Ar or 5 vol% O_2/Ar mixture introduced in pulsed mode condition.

3. Results and discussion

3.1. Structural features of FSM-16 support

To investigate the structure of FSM-16, Fig. 1A and 1 B showed the N$_2$ adsorption isotherms and pore size distributions of FSM-16. Using the IUPAC classification, FSM-16 displayed a type IV sorption isotherm with a sharp capillary condensation step in the relative pressure (p/p_0) range of 0.3–0.6. With respect to the pore size distributions of FSM-16, a sharp peak was observed (Fig. 1B), which suggested that there were uniform mesopores with the most probable diameter (D_p) at approximately 2.10 nm. As listed in Table 1, the BET surface area (S_{BET}) and total pore volume (V_t) were 1079 m^2/g and 1.08 cm^3/g, respectively. The small-angle XRD pattern of FSM-16 was shown in Fig. 1C. It could clearly be seen that there were
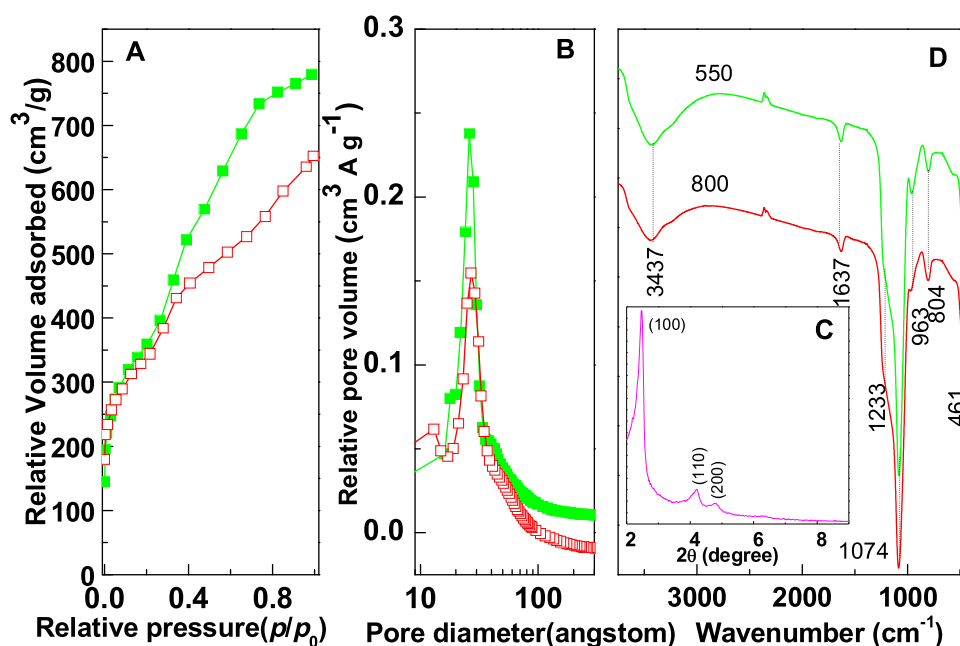
Fig. 1. (A) Nitrogen adsorption isotherms and (B) pore size distributions of FSM-16 calcined at (■) 550 °C and (□) 800 °C; (C) small-angle XRD pattern of FSM-16 calcined at 550 °C; (D) FT-IR spectra of FSM-16.

Table 1
Physical properties of support, fresh and used sorbents.

Sample	S_{BET}	(m²/g)	V_t(mm³/g)		V_{mic}(mm³/g)	V_{mec}(mm³/g)	D_a(nm)
FSM-16		1079	1080	340		740	4.02
FSM-16 calcined at 800 °C		791	740	270		470	3.74
4Mn1Fe/FSM-16		315	240	100		140	3.10
4Mn1Fe-3%Mo/FSM-16		340	280	90		180	3.23
4Mn1Fe-10%Mo/FSM-16		332	290	80		210	3.46
4Mn1Fe-25%Mo/FSM-16		196	140	50		80	2.80
S-4Mn1Fe-3%Mo/FSM-16		110	110	10		100	4.04
S-4Mn1Fe-10%Mo/FSM-16		93	100	20		80	3.58
S-700-4Mn1Fe-3%Mo/FSM-16		70	80	20		60	4.74
S-4Mn1Fe-3%Mo/FSM-16(39.6%H₂)		98	90	20		70	3.83
S-4Mn1Fe-3%Mo/FSM-16(39.6%H2,32%CO)		78	100	30		70	4.97
R8-4Mn1Fe-3%Mo/FSM-16		65	70	10		60	4.31

The physical parameters of all samples were calculated using the BJH method.

three distinct peaks at $2\theta = 2.48$ ($d = 3.56$ nm), 4.20 and 4.77°, which were attributed to the (100), (110) and (200) reflections of the two-dimensional (2-D) hexagonal structure (p6 mm space group) [28,32]. Based on the d-spacing of (100) crystal plane (Fig. 1C), the pore wall thickness ($h = 2.01$ nm) of FSM-16 was calculated from the difference between unit cell constant ($a_0 = 2d_{100}/3^{0.5}$) and the most probable diameter ($D_p = 2.10$ nm). These results provided an evidence for the formation of long-range-order structure as reported in previous work [28,33].

In order to assess the thermal stability of FSM-16 at high temperature, Fig. 1A illustrated that the N₂ adsorption isotherm of FSM-16 after calcination at 800 °C for 6 h did not vary remarkably except that the amount of N₂ adsorption reduced and the pore size distribution was broadened slightly. In the meantime, the S_{BET} and V_T decreased slightly in relative to FSM-16 calcined at 550 °C (Table 1). The FT-IR spectrum of FSM-16 was shown in Fig. 1D. The broad absorption band at 3437 cm⁻¹ is from the stretching vibration of the surface hydroxyl groups and the band at 1637 cm⁻¹ is associated with bending vibration of hydroxyl groups (-Si-OH) (Fig. 1D). The weak band at 963 cm⁻¹ is ascribed to defect sites (=Si-OH) [34] while those at 1000–1400 cm⁻¹ and 400–900 cm⁻¹ correspond to asymmetric and symmetric stretching vibration of Si-O-Si bridges, respectively [35]. After calcination at 800 °C, there was no apparent

change in the position and intensity of the peaks, which indicated that the structure of FSM-16 was well maintained. It was similar to the aforementioned observation in the N₂ adsorption isotherms. Thus, it was quite apparent that FSM-16 could withstand the high temperature requirement stipulated by hot coal gas desulfurization process.

3.2. Characterization of sorbents

3.2.1. XRD analysis

Wide-angle XRD patterns of the fresh, used and regenerated sorbents were shown in Fig. 2. It could be seen that no silicate signals were observed for all sorbents, which illustrated that the interaction between metal oxides and FSM-16 was very weak. For fresh 50% 4Mn1Fe/FSM-16 sorbent (Fig. 2a), $Mn_{2-x}Fe_xO_3$ ($2\theta = 23.1$, 32.9, 38.2, 55.1 and 65.7°) [PDF#24-0507] was the main crystal phase due to the fact that Fe^{3+} ion was inserted into the lattice of cubic Mn_2O_3 and occupied the position of Mn^{3+}. This lattice replacement did not affect the main structure of manganese oxide. In addition, it was also accompanied with the formation of tetragonal structural Mn_3O_4 ($2\theta = 36.07°$). According to the equilibrium diagram of Mn-O system, a small amount of Mn_3O_4 may come from the decomposition of MnO_2 during
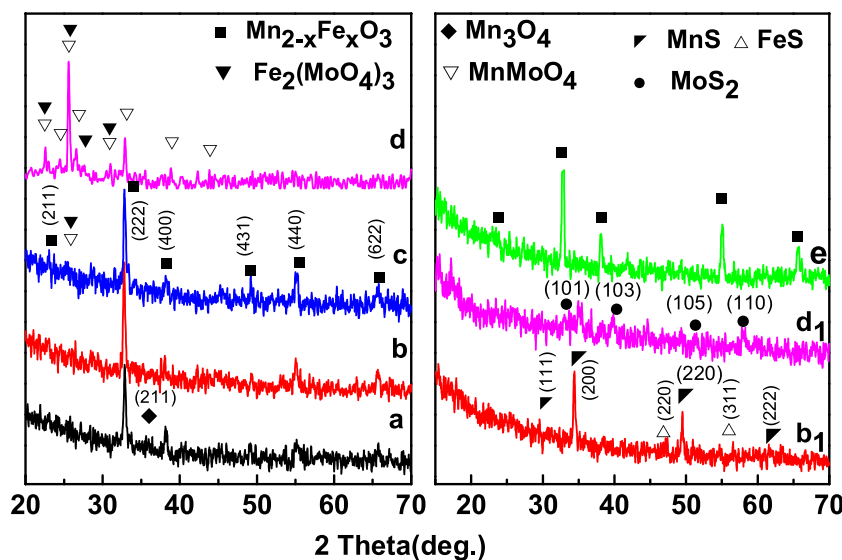
Fig. 2. XRD patterns of (a) fresh 50% 4Mn1Fe/FSM-16, (b, b$_1$) fresh and used 50% 4Mn1Fe-3%Mo/FSM-16, (c) 50% 4Mn1Fe-10%Mo/FSM-16, (d, d$_1$) fresh and used 50% 4Mn1Fe-25%Mo/FSM-16, and (e) 8th regenerated 50% 4Mn1Fe-3%Mo/FSM-16.

calcination at high temperature. Due to very low loading of Mo species, no peaks corresponding to MoO$_x$ were observed in the pattern of fresh 50% 4Mn1Fe-3%Mo/FSM-16. However, for the 50% 4Mn1Fe-10%Mo/FSM-16, the characteristic diffraction peaks of manganese molybdate (MnMoO$_4$ [PDF#50-1287]) and ferric molybdate (Fe$_2$(MoO$_4$)$_3$ [PDF#31 −0642]) were observed except for the phase of Mn$_{2-x}$Fe$_x$O$_3$. As shown in Fig. 2d, when the loading of Mo was 25%, the diffraction peaks of Mn$_{2-x}$Fe$_x$O$_3$ disappeared and those of MnMoO$_4$ and Fe$_2$(MoO$_4$)$_3$ intensified, which was because that Mn^{2+}(4s^{0}3d^5) and Mo^{6+}(4d^0) ions in the crystal structure of MnMoO$_4$ had the most stable electronic configurations and that the interaction between MoO$_3$ and Fe$_2$O$_3$ could easily form Fe$_2$(MoO$_4$)$_3$ due to the occupation of surface vacant sites of Fe$_2$O$_3$ by Mo^{6+} ions [36,37]. After sulfidation at 600 °C, there were the diffraction peaks of MnS (2θ = 29.6, 34.3, 49.3 and 61.5°) and FeS (2θ = 47.5 and 56.2°) [PDF#23-1123] in the XRD pattern of 50% 4Mn1Fe-3%Mo/FSM-16 sorbent, indicating the conversion of metal oxides to metal sulfides. Only weak MoS$_2$ [PDF#37-1492] peaks at 2θ = 33.5, 39.6 and 58.4° could be detected over used 50% 4Mn1Fe-25%Mo/FSM-16. After eighth successive sulfidation/regeneration cycles, Mn$_{2-x}$Fe$_x$O$_3$ phase was restored (Fig. 2e) and there were no diffraction peaks of sulfates, suggesting that the sorbent could be regenerated completely. The intensity of diffraction peaks was similar to the fresh one, which indicated that high dispersion of active constituent on the surface of FSM-16 was still maintained after multiple cycles.

3.2.2. BET analysis

The N$_2$ adsorption and pore size distribution over fresh and used sorbents were shown in Fig. 3, the results indicated that after metal oxides were introduced, the mesoporous structure of all fresh sorbents almost remained intact. As listed in Table 1, both S_{BET} and V_t of fresh sorbents decreased remarkably when compared with FSM-16 material, which was due to the fact that the nano-sized metal oxides occupied the channels of FSM-16. However, the S_{BET} and V_p over 50% 4Mn1Fe-3%Mo/FSM-16 and 50% 4Mn1Fe-10%Mo/FSM-16 sorbents were slightly higher than these over 50% 4Mn1Fe/FSM-16. It revealed clearly that when a small amount of Mo was added, the dispersion of active components on the surface of FSM-16 was improved and the numbers of active sites were increased, leading to higher reactivity towards H$_2$S. When the loading of Mo was increased to 25% (Fig. 3A), the mesoporous structure

of sorbent almost disappeared due to the formation of MnMoO$_4$ and Fe$_2$(MoO$_4$)$_3$ with large molecular size that blocked the partial channels. For the used sorbents, because the radius of S^{2-} ion (0.184 nm) is larger than that of O^{2-} ion (0.14 nm), when the metal oxides were transformed into metal sulfides, it leaded to a drastic decline in S_{BET} and V_t. Moreover, S_{BET} and V_t could be further reduced when the sulfidation temperature was increased, which could be explained by two factors: (i) high-temperature treatment caused serious shrinkage of mesopores, resulting in smaller pore diameter and lower surface area[38], and (ii) partial sintering of active species at high temperature.

3.2.3. HRTEM images of sorbents

Detailed structural and morphology of FSM-16 can be observed on a microscopic scale via TEM. As shown in Fig. 4a, the HRTEM image of FSM-16 exhibited well-ordered hexagonal array of mesopores when the electron beam was parallel to pore direction, while the electron beam was perpendicular to the main axis of the cylindrical pores, clear lattice fringes could be seen, indicating a highly ordered 2D pore structure. The distance between two dark strips, estimated to be about 2.86 nm using the magnification image (Fig. 4b), was very close to the most probable pore diameter (Fig. 1B). The fast Fourier transform (FFT) pattern (Fig. 4d) showed an array of ordered bright spot characteristics, which suggested the existence of single-channel structure. Energy dispersive X-ray spectroscopy (EDX) analysis (Fig. 4c) showed that the atomic percentages of Si and O were 39.06% and 60.94%, respectively, i.e. O/Si atomic ratio in FSM-16 was about 2, which proved the FSM-16 consisted of SiO$_2$. The distance between two pore-walls obtained from FFT was 2.6 nm, which was consistent with the results gained from N$_2$ adsorption and small-angle XRD.

The HRTEM images of fresh 50% 4Mn1Fe-3%Mo/FSM-16 sorbent were shown in Fig. 5. After loading with the metal oxides, the lattice fringes of FSM-16 could be seen clearly and there was no apparent aggregation of metal oxides, which revealed that mesoporous structure of FSM-16 remained intact and the active constituents were dispersed uniformly in the channels of FSM-16 (Fig. 5a). EDX analysis (Fig. 5b) verified that the molar ratio of Mn/Fe was 3.67:1 and the loading of Mo was 2.59%, which was close to the stoichiometric value, demonstrated that Mn, Fe and Mo oxides were incorporated successfully into FSM-16. Fig. 5c showed the SAED pattern of metal oxides in fresh 50% 4Mn1Fe-3%Mo/FSM-16 and the
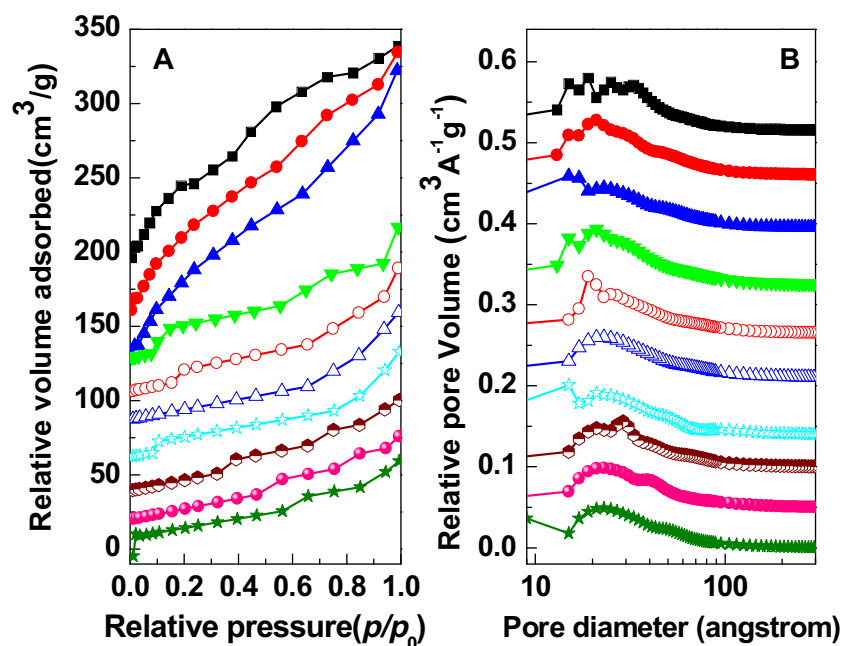
Fig. 3. N_2 adsorption isotherms (A) and pore size distribution of (■) fresh 50% 4Mn1Fe/FSM-16; (●, ○) fresh and used 50% 4Mn1Fe-3%Mo/FSM-16; (B) (▲, △) fresh and used 50% 4Mn1Fe-10%Mo/FSM-16, (▼) fresh 50% 4Mn1Fe-25%Mo/FSM-16; (☆) used 50% 4Mn1Fe-3%Mo/FSM-16 (39.6%H_2); (◗) used 50% 4Mn1Fe-3%Mo/FSM-16 (39.6% H_2, 32% CO); (●) 50% 4Mn1Fe-3%Mo/FSM-16 regenerated at 700 °C after eight cycles; (★) 50% 4Mn1Fe-3%Mo/FSM-16 used at 700 °C.
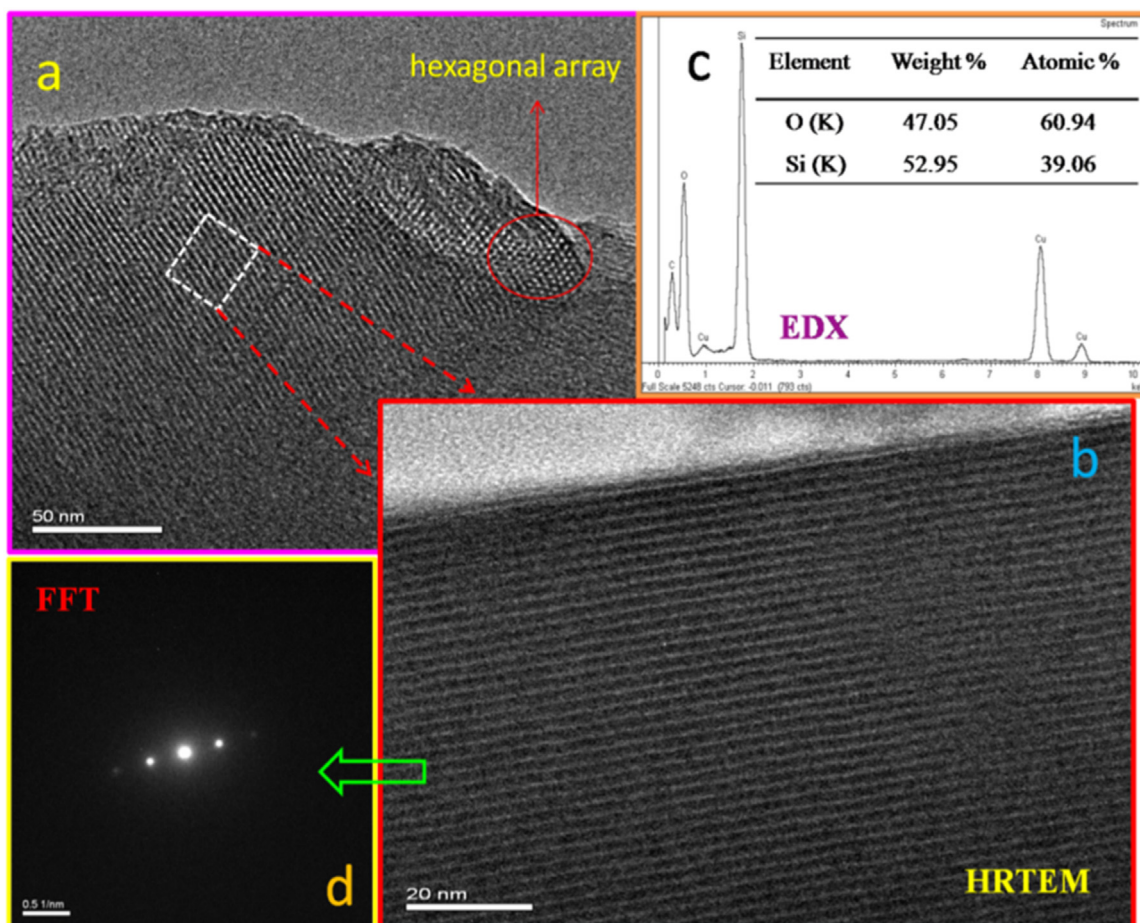

Fig. 4. HRTEM images (a and b) of FSM-16 in a direction perpendicular and parallel to the channels; (c) the corresponding EDX analysis; (d) FFT pattern.
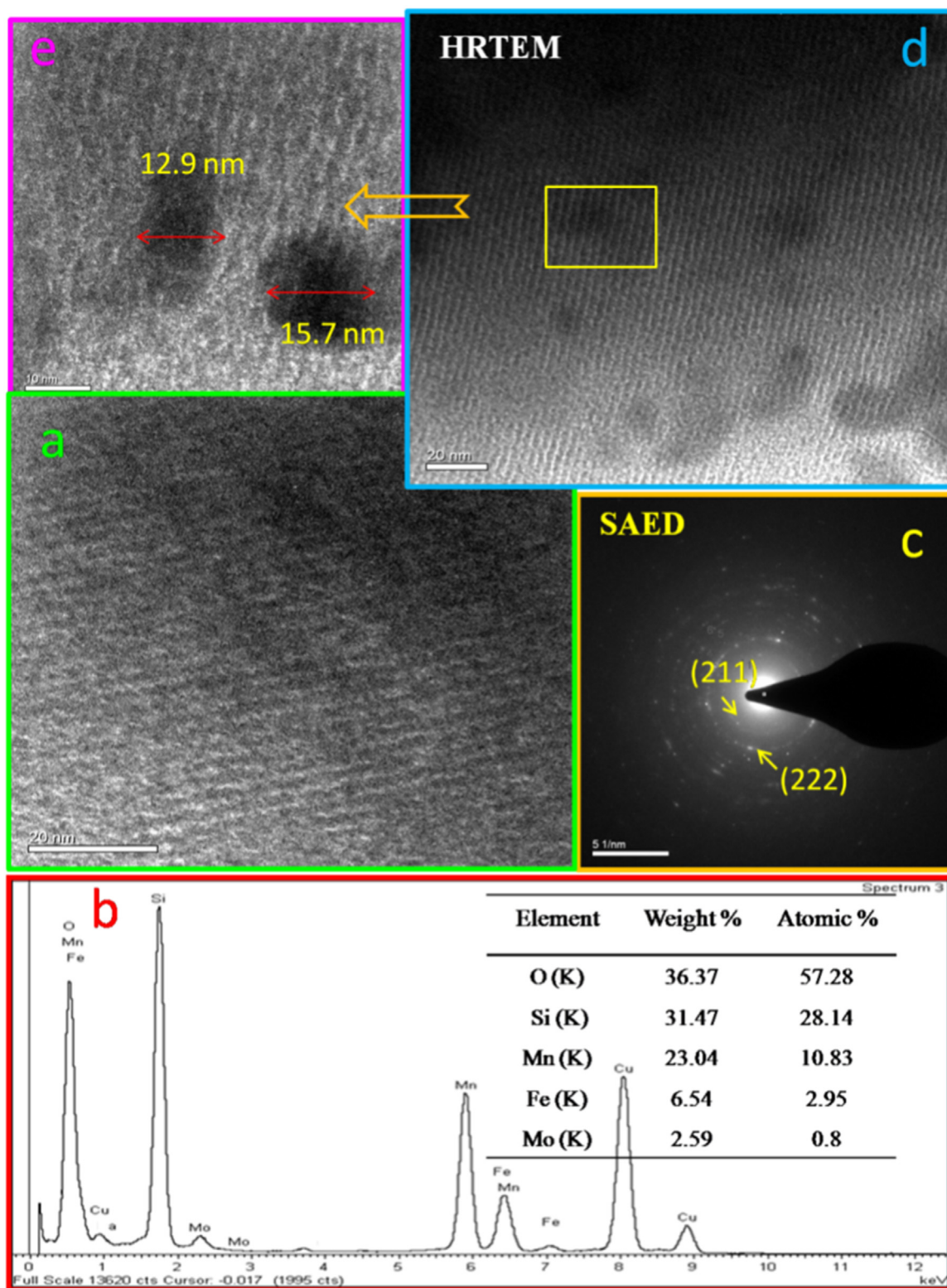
Fig. 5. (a) and (d) HRTEM images of fresh 50% 4Mn1Fe-3%Mo/FSM-16; (e) high magnification HRTEM image; (b) the corresponding EDX analysis of fresh sorbent; (c) SAED pattern of the metallic oxides in fresh 50% 4Mn1Fe-3%Mo/FSM-16.

weak dispersive circles indicated the nanosized metal oxide particles were small and mainly existed in polycrystallites. The distances between lattice planes of the crystal were measured to be 0.38 and 0.27 nm *via* the SAED patterns, which were in accord with (211) and (222) lattice spacing of $Mn_{2-x}Fe_xO_3$. This result further confirmed the conclusion of XRD analysis (Fig. 2b). No signal of Mo species

was observed in SAED image, which was reasonable because the loading was low. In addition, as shown in Fig. 5d, owing to high loadings of active component (50%) in the sorbents during preparation, a small amount of metal oxides was aggregated on the outer surface of FSM-16 with diameters of ca. 10–15 nm.
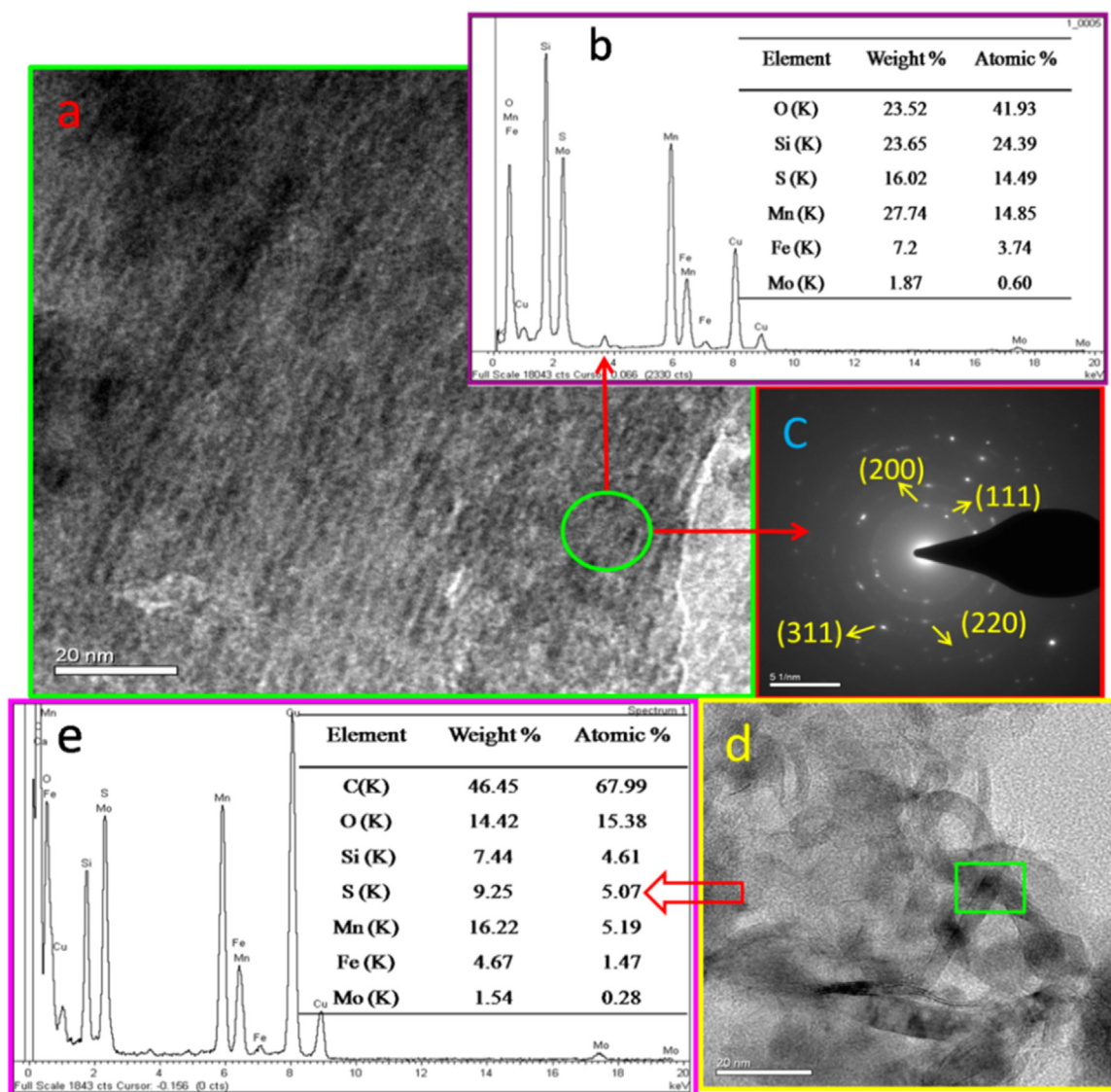
Element	Weight %	Atomic %
O (K)	23.52	41.93
Si (K)	23.65	24.39
S (K)	16.02	14.49
Mn (K)	27.74	14.85
Fe (K)	7.2	3.74
Mo (K)	1.87	0.60

Element	Weight %	Atomic %
C(K)	46.45	67.99
O (K)	14.42	15.38
Si (K)	7.44	4.61
S (K)	9.25	5.07
Mn (K)	16.22	5.19
Fe (K)	4.67	1.47
Mo (K)	1.54	0.28

Fig. 6. (a, d) HRTEM images; (b, e) corresponding EDX analysis and (c) SAED pattern of 50% 4Mn1Fe-3%Mo/FSM-16 after sulfidation at 600 °C.

Fig. 6 depicted clearly the stripe structure of used 50% 4Mn1Fe-3%Mo/FSM-16, indicating that FSM-16 remained intact after sulfidation at 600 °C. Moreover, since no significant aggregation of metal sulfides was observed, it indicated that FSM-16 was effective in suppressing the migration of active particles. EDX analysis (Fig. 6b) exhibited the existence of large amounts of sulfur, verifying the transformation of metal oxides to metal sulfides after desulfurization. Besides, the diffraction spots of polycrystallites in the SAED image became brighter compared to fresh 50% 4Mn1Fe-3%Mo/FSM-16, which revealed the growth of crystallites of sulfides or slight agglomeration after sulfidation reaction. The crystal d-spacing calculated from SAED image were 0.33 nm, 0.25 nm, 0.21 nm and 0.17 nm, respectively. The former two were in accord with the (111) and (200) planes of cubic MnS crystallites and the rest were attributed to the (220) and (311) planes of FeS, respectively. It was interesting to note that, some nanofibers were formed on the surface of sulfided sorbent in some regions (Fig. 6d). Corresponding EDX analysis verified that there were large amounts of layered carbon species as well as Si, O, Mn, Fe and Mo elements in these regions (Fig. 6e). The formation of graphenic carbon layer was plausible from the disproportionation reaction of CO, which was further confirmed by the TOF-MS results hereinafter.

3.2.4. H_2-TPR measurements

In H_2S removal process, the reduction behavior of metal oxides seriously affected the desulfurization performance of sorbents. To investigate the reducibility of the sorbents at the reducing atmosphere, the H_2-TPR profiles of sorbents containing different active components were shown in Fig. 7. It could be seen that there were two obvious reduction peaks at 393 °C and 561–642 °C in the profile of 50% Fe/FSM-16 (Fig. 7a). The former was ascribed to the reduction of Fe_2O_3 to Fe_3O_4 and the latter was attributed to the reduction of Fe_3O_4 and FeO to Fe [39–41]. The following equations describe the reduction reaction of the Fe species:

$$3Fe_2O_3 + H_2 = 2Fe_3O_4 + H_2O \tag{2}$$

$$Fe_3O_4 + H_2 = 3FeO + H_2O \tag{3}$$

$$FeO + H_2 = Fe + H_2O \tag{4}$$

In addition, the weak peak at 315 °C was assigned to the reduction of highly dispersed ferric oxides. The smaller oxide particles have more exposed surface oxygen, which can react readily with hydrogen at low temperature. As for the 50% Mn/FSM-16 (Fig. 7b), two well-separated peaks at 367 °C and 441 °C revealed two-step conversion of Mn_2O_3 to Mn_3O_4 and then to MnO [42]. The H_2-
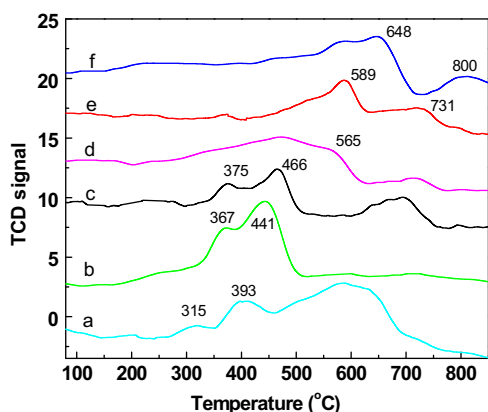
Fig. 7. H_2-TPR profiles for fresh (a) 50% Fe/FSM-16; (b) 50% Mn/FSM-16; (c) 50% 4Mn1Fe/FSM-16; (d) 50% 4Mn1Fe-3%Mo/FSM-16; (e) 50% 4Mn1Fe-10%Mo/FSM-16; (f) 50% 4Mn1Fe-25% Mo/FSM.

TPR profile over 4Mn1Fe/FSM-16 (Fig. 5c) was different from these over 50% Mn/FSM-16 and 50% Fe/FSM-16, implying the formation of $Mn_{2-x}Fe_xO_3$ phase, as confirmed by the wide-angle XRD results. As shown in Fig. 7d-f, the incorporation of Mo significantly affected the reduction behavior of Mn-Fe sorbents. When the amount of Mo species increased steadily, the first peak decreased gradually in intensity and finally submerged into the second peak. The XRD results verified the existence of $MnMoO_4$ and $Fe_2(MoO_4)_3$ in 4Mn1Fe-25%Mo/FSM-16. This meant that the following reactions would occur:

$$MnMoO_4 = MnO + MoO_3 \tag{5}$$

$$MoO_3 + H_2 = MoO_2 + H_2O \tag{6}$$

As reported in literature[43], MnO could not be further reduced to elemental manganese at a temperature lower than 1200 °C under reduction atmosphere. Therefore, the peak at 648 °C in 50% 4Mn1Fe-25% Mo/FSM-16 could be attributed to the reduction of MoO_3 [44]. The peak at 800 °C was related to the reduction of $Fe_2(MoO_4)_3$ phase [37]. In the TPR profiles of all Mo incorporated

sorbents, the positions of all reduction peaks of Fe species were shifted continuously to high temperature with the increment of Mo content. This was because that the charge transfer between Fe and Mo led to an electron-deficient state of Fe species and promoted more core-level electron density of Fe nuclei to take part in Fe-O covalent bonds, which made the removal of oxygen more difficult during reduction. As a consequent, the reduction ability of 50% 4Mn1Fe-xMo/FSM-16 was restrained greatly with the incorporation of Mo species.

3.2.5. UV–vis diffuse reflectance spectroscopy (UV-DRS)

UV–vis DRS can provide the information regarding the valence state of active particles and their chemical environment. Fig. 8A showed UV–vis spectra of Mn-based sorbents and FSM-16 as a reference. The spectra of Mn-based sorbents correspond to those reported previously for binary oxide systems such as Mn-LDH [45] and Mn-Ti [46]. The spectrum of 50% Mn/FSM-16 exhibited three main absorption bands at ca. 387, 534 nm as well as a weak shoulder around 750 nm. Based on the report of Velu et al. [45], the bands around 387 nm and 534 nm were related to the charge transfer and the d-d transfer transitions of Mn_2O_3. They were assigned to $O^{2-} \rightarrow Mn^{3+}$ charge transfer transition superimposed on the $^5B_{1g} \rightarrow {}^5B_{2g}$ and $^5B_{1g} \rightarrow {}^5E_g$ crystal field d-d transitions, respectively. The weak shoulder around 750 nm was due to the $^5B_{1g} \rightarrow {}^5A_{1g}$ d-d transition in the Mn^{3+} ion. The DRS results suggested that the manganese oxide was mainly in the form of Mn_2O_3. As for the 50% 4Mn1Fe/FSM-16, the absorption peaks were not changed significantly and no characteristic bands of iron oxides were observed, which illustrated that iron oxides were highly dispersed in the Mn_2O_3 structure. This conclusion was confirmed by the formation of solid solution ($Mn_{2-x}Fe_xO_3$ phase). In addition, it was easily noted that the DRS bands shifted slightly towards lower wavelength side for sorbents containing Mo, which implied that there was an enhancement of band gap energy as a result of interaction with Mo species. According to quantum-mechanical theory, the band gap energy is inversely proportional to the size of nanoparticles. One could deduce that as the content of Mo species increased, the particle size of the metal oxides gradually decreased. However, the characteristic bands of manganese oxides almost vanished
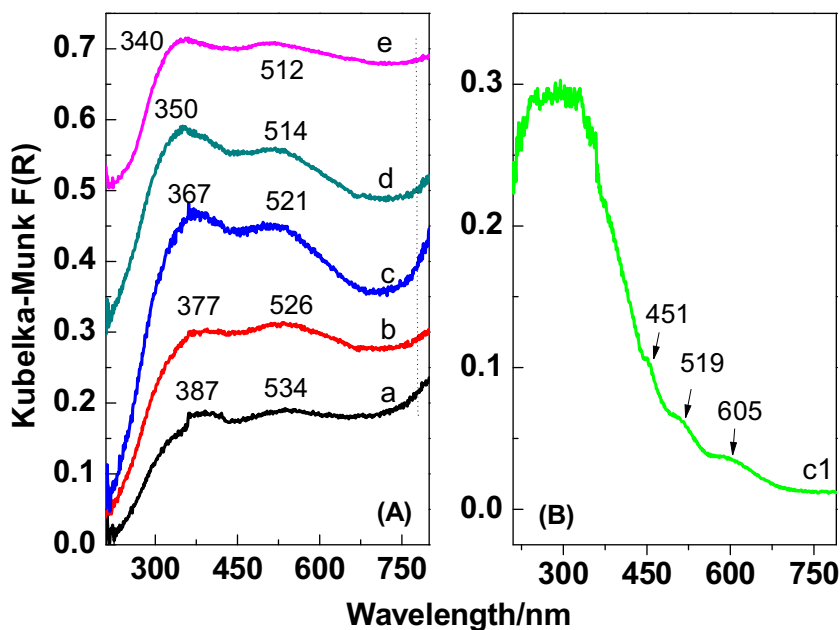

Fig. 8. UV–vis DRS of the powders (a) 50% Mn/FSM-16, (b) 50% 4Mn1Fe/FSM-16, (c) 50% 4Mn1Fe-3%Mo/FSM-16, (d) 50% 4Mn1Fe-10%Mo/FSM-16 and (e) 50% 4Mn1Fe-25%Mo/FSM-16, (B) used 50% 4Mn1Fe-3%Mo/FSM-16.
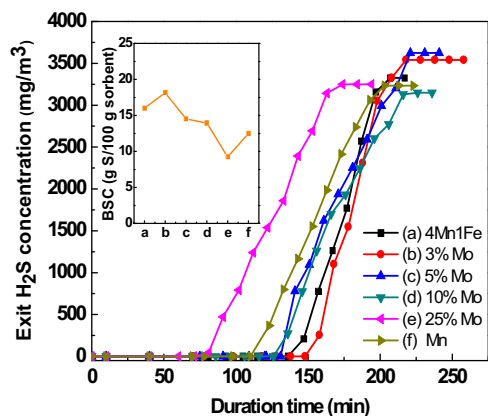
Fig. 9. Desulfurization behavior over different 50% 4Mn1Fe-x%Mo/FSM-16 at 700 °C, (a) 50% 4Mn1Fe/FSM-16 (b) 50% 4Mn1Fe-3%Mo/FSM-16 (c) 50% 4Mn1Fe-5%Mo/FSM-16 (d) 50% 4Mn1Fe-10%Mo/FSM-16, (e) 50% 4Mn1Fe-25%Mo/FSM-16 and (f) 50% Mn/FSM-16 ($WHSV$ = 9 × 10^3 mL h^{-1} g^{-1}; Feed composition: 0.33% H$_2$S, 10.5% H$_2$, 18% CO and N$_2$ balance gas).

for the 50% 4Mn1Fe-25%Mo/FSM-16, suggesting the transitions to manganese molybdate compound. As for used sorbent, the peaks at 451 nm, 519 nm and 605 nm could be assigned to $^6A_{1g} \rightarrow {}^4A_{1g}$, $^6A_{1g} \rightarrow {}^4T_{2g}$ and $^6A_{1g} \rightarrow {}^4T_{2g}$ d–d transitions of Mn^{2+}(d^5) either in octahedral or tetrahedral crystal field [45,47], indicating the sulfurization of Mn$_2$O$_3$ to MnS.

3.3. H$_2$S removal activity evaluation of sorbents

The effect of Mn/Fe/Mo contents on the desulfurization performance of sorbents was showed in Fig. 9. It was easily seen that 50% Mn/FSM-16 exhibited low BSC (12.49 g S/100 g sorbent) with a slow deactivation rate (Fig. 9f). As reported previously, the low BSC was due to the existence of large Mn$_2$O$_3$ crystallites when no additives were added, which increased the diffusion resistance of H$_2$S gas from the surface to bulk [48]. However, this sulfur capacity was still much higher than that of single manganese oxide supported on activation carbon or γ-Al$_2$O$_3$ [49,50]. Fig. 9a showed that the formation of Mn$_{2-x}$Fe$_x$O$_3$ solid solution increased remarkably the BSC of Mn-based sorbent and rapid deactivation or the maximum utilization of sorbent was reached after the breakthrough time point. Interestingly, the desulfurization performance of Mo modified Fe-Mn/FSM-16 sorbent increased initially and then declined as the Mo content increased beyond 3%. The 50% 4Mn1Fe-3%Mo/FSM-16 sorbent exhibited the highest BSC (18.15 g S/100 g sorbent) at 600 °C, which was the best result reported on supported sorbents up to date. The N$_2$ adsorption and H$_2$-TPR results of the sorbent also indicated that the introduction of molybdenum species effectively improved the dispersion of particles and restrained the reduction of Mn$_2$O$_3$ and Fe oxides, which was favorable for the removal of H$_2$S. As for 50% 4Mn1Fe-25%Mo/FSM-16, the BSC was very low, plausibly due to the formation of a dense MoS$_2$ and Mo$_2$C layers on the surface of the sorbent during desulfurization. These layers increased diffusion resistance of gas molecules and limited the sulfidation reaction between active constituent in bulk and H$_2$S [20,23]. Therefore, high Mo loading was disadvantageous to the enhancement of sulfur capacity.

The effect of temperature on the desulfurization performance of sorbent was investigated in the range of 550–700 °C. As shown in Fig. 10, as temperature increased from 550 to 600 °C, the breakthrough time was prolonged. From kinetics point of view, the sulfidation reaction is controlled by the reaction rate of H$_2$S with active components (S/O exchange) and gas diffusion efficiency (H$_2$S and H$_2$O) [51]. According to the report of Bakker et al. [52], these
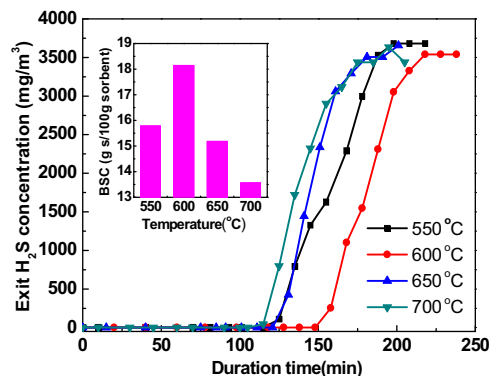

Fig. 10. H$_2$S breakthrough curves and breakthrough sulfur capacity over 50% 4Mn1Fe-3%Mo/FSM-16 at different temperature. ($WHSV$ = 9 × 10^3 mL h^{-1} g^{-1}; Feed composition: 0.33% H$_2$S, 10.5% H$_2$, 18% CO and N$_2$ balance gas).
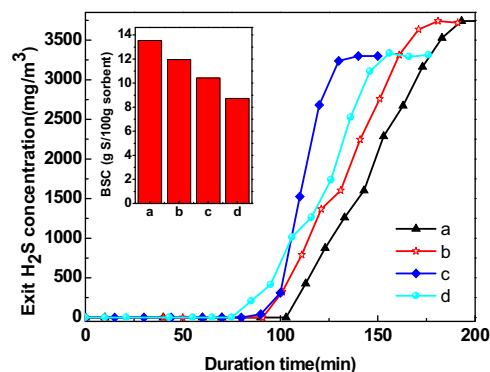

Fig. 11. Effect of gas composition on H$_2$S breakthrough curves over 50% 4Mn1Fe-3% Mo/FSM-16: (a) 39.6% H$_2$, 18% CO; (b) 39.6% H$_2$, 32% CO; (c) 10.5% H$_2$, 18% CO, 5% steam; (d) 39.6% H$_2$, 32% CO, 5% steam. ($WHSV$ = 9 × 10^3 mL h^{-1} g^{-1}; 0.33% H$_2$S and N$_2$ balance gas).

factors are strongly dependent on the temperature in a particular range. The best desulfurization performance was obtained at 600 °C with a maximum BSC of 18.15 g S/100 g sorbent, which exhibited the best combination of gas diffusion and S/O exchange. When the sulfidation temperature was increased to 700 °C, the BSC dropped significantly. This was attributed to the reduction of ferric oxides under reducing gas environment, which has been recognized that the reduction of ferric oxides enhanced in the presence of H$_2$ and CO at high temperature, leading to the formation of wustite (Fe$_{0.947}$O) and even metallic Fe [24]. The activity of these species towards H$_2$S was low compared to magnetite, which resulted in a sorbent with lower reactivity. In the meantime, with an increase in temperature, partial sintering of the sorbent resulted in the decline of surface area and pore volume of the sorbent (Table 1, at 700 °C). The sintering effect hindered severely gas diffuse into the bulk of the sorbent, resulting in a decline of desulfurization performance.

3.4. Effect of gas composition on desulfurization performance

In general, the raw gas from gasification of coal contains a large amount of reduction gas (H$_2$ and CO) and small quantities of water vapor, which affects not only the structural stability but also the desulfurization performance of sorbents. Therefore, it is necessary to assess the reducing atmosphere-resistance and H$_2$O-resistance abilities of sorbents for industrial applications. The desulfurization performance of 50% 4Mn1Fe-3%Mo/FSM-16 in different simulated gases was shown in Fig. 11. When the concentration of H$_2$ increased from 10.5% (Fig. 9b) to 39.6% (Fig. 11a), the BSC of the sorbent reduced about 25%. Due to the presence of excessive H$_2$, Mn$_2$O$_3$
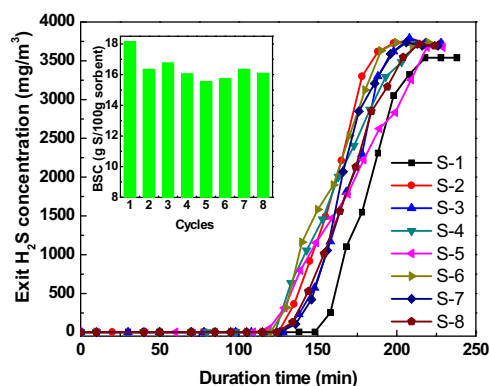
Fig. 12. Sulfurization-regeneration cycles over 50% 4Mn1Fe-3% Mo/FSM-16. Sulfurization: 600 °C; $WHSV = 9 \times 10^3$ mL h^{-1} g^{-1}; 0.33% H_2S, 10.5% H_2, 18% CO, and N_2 balance. Regeneration: 700 °C; $WHSV = 9 \times 10^3$ mL h^{-1} g^{-1}; 5% O_2/N_2 mixture, inset is the breakthrough sulfur capacity.

and Fe_2O_3 were readily reduced to oxides with low valence, which was unfavorable for the desulfurization process. In addition, when the amount of CO increased from 18% to 32% (Fig. 11a-b) with a constant amount of H_2S, the BSC only decreased slightly. Liu et al. [14] reported earlier, the reversed water-gas shift reaction $(CO(g) + H_2O(g) \rightarrow CO_2(g) + H_2(g))$ favored the occurrence of sulfidation reaction in the presence of CO, which consumed H_2O and the chemical equilibrium of sulfidation reaction shifted toward the positive direction. This compensated the decrease in BSC that was caused by the reducing action of CO to some extent. It was easily seen that the BSC over 50% 4Mn1Fe-3%Mo/FSM-16 was significantly higher than that reported by Yu et al. [20] at similar gas composition. In addition, in order to evaluate the H_2O-resistance ability of 50% 4Mn1Fe-3%Mo/FSM-16 sorbent, 5 vol% steam was added to the simulated gases and the results were shown in Fig. 11c-d. It could be seen that the BSC was 10.43 g S/100 g sorbent, about 57.47% of the initial BSC value obtained without water. The main sulfidation reaction occurred under water containing atmosphere is following:

$$Me_xO_y(s) + yH_2S(g) \leftrightarrow yMe_{(x/y)}S(s) + yH_2O(g) \tag{7}$$
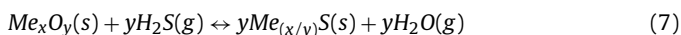
H_2O, as a product of sulfidation reaction, drives the equilibrium to the left, which leads to a decrease in BSC. Consequently, when water vapor was presented, it greatly suppressed the sulfidation reaction as given in Eq. (7). However, when water vapor was presented in strong reducing coal gas, the sulfur capacity over 50% 4Mn1Fe-3%Mo/FSM-16 declined by only 27% of that obtained without water vapor, which was likely that the adverse effect of H_2O on sulfidation was weaken by the reversed water-gas shift reaction.
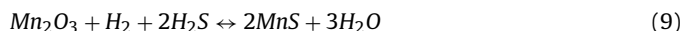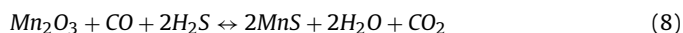
3.5. Regeneration performance of 50% 4Mn1Fe-3%Mo/FSM-16

Regeneration and long-term stability of the sorbents are vital properties in practical H_2S removal. To evaluate these properties of 50% 4Mn1Fe-3%Mo/FSM-16, eight consecutive desulfurization-regeneration cycles were carried out. Regeneration conditions were chosen based on the previous report [53]. Low temperature (<600 °C) can result in the formation of sulfate, which was unfavorable for regeneration. The low contents of oxygen in the regeneration stream effectively limited the sulfate formation and avoided sintering caused by lots of heat. Therefore, the used sorbent was regenerated in 5% O_2/N_2 mixtures at 700 °C. As shown in Fig. 12, the breakthrough curves of regenerated sorbents were very close to that of the fresh sorbent. There was a slight decrease in BSC after the first regeneration cycle, which was 90.05% of the initial sulfur capacity. After that, a minor fluctuation between

15.56–16.75 g S/100 g sorbent was observed. The loss of sulfur capacity could be attributed to partial sintering of the sorbents and slight aggregation of active species due to strong heat release in regeneration process. The XRD results showed that the sorbent after the eighth regenerated cycle (Fig. 2e) was as good as the fresh one except the peak had minor enhancement in intensity, which indicated that 50% 4Mn1Fe-3%Mo/FSM-16 could be completely regenerated. After multiple sulfidation/regeneration cycles, there was no phenomenon of pulverization and the desulfurization property was well maintained. As a result, this sorbent synthesized from relatively low cost raw material offers promising solutions for industrial applications in the near future.

3.6. Identification of sulfidation/regeneration mechanism by in situ TOF-MS

It is a challenging and crucial scientific issue to understand properly the sulfur/oxygen-exchange mechanism during the hot coal gas desulfurization. The highly sensitive in situ TOF-MS technique has been used to investigate the process of H_2S removal and the regeneration mechanism of used 50% 4Mn1Fe-3%Mo/FSM-16 sorbent. TOF-MS signals over 50% Mn/FSM-16, 50% 4Mn1Fe/FSM-16 and 50% 4Mn1Fe-3%Mo/FSM-16 sorbents were shown in Fig. 13. As shown in Fig. 13A, the weak peaks of H_2O^+ ($m/z = 18$) and CO_2^+ ($m/z = 44$) were observed and H_2^+ and CO^+ signals decreased gradually at the beginning of the reaction over 50% Mn/FSM-16 sorbent, which indicated that Mn_2O_3 was initially reduced to MnO, and followed by a sulfidation reaction to form MnS in a reducing atmosphere. The reactions can be represented by Equations (8) and (9):

$$Mn_2O_3 + CO + 2H_2S \leftrightarrow 2MnS + 2H_2O + CO_2 \tag{8}$$

$$Mn_2O_3 + H_2 + 2H_2S \leftrightarrow 2MnS + 3H_2O \tag{9}$$

In our previous desulfurization reaction, only MnS was identified in sulfided sorbents by the XRD analysis, which revealed that reduction reactions occurred initially, subsequently, the sulfidation reaction indeed happened during desulfurization. As the reaction proceeds, the peak at $m/z = 44$ firstly weaken in intensity with the exhaustion of Mn_2O_3 in the sorbent and then increased remarkably and companied with the presence of C^+ signal due to the disproportionation reaction of CO. The desulfurization process was allowed to proceed for 140 min, the peaks of S^+ ($m/z = 32$) and H_2S^+ ($m/z = 34$) were observed, which indicated that the desulfurization process was nearly finished. The peak of S^+ was attributed to the decomposition of COS, which could be inferred from the side reaction between H_2S and CO or CO_2 according to the following reactions:

$$H_2S + CO \leftrightarrow COS + H_2 \tag{10}$$

$$H_2S + CO_2 \leftrightarrow COS + H_2O \tag{11}$$

However, no COS signal was observed before the breakthrough time of H_2S, which demonstrated that COS and H_2S could be removed simultaneously by Mn-based sorbents ($MnO + COS \leftrightarrow MnS + CO_2$). In addition, the peak at $m/z = 12$ indicated the formation of C^+ after the breakthrough of H_2S, which was produced by two pathways as follows:

$$2CO \leftrightarrow C + CO_2 \tag{12}$$

$$CO + H_2 \leftrightarrow C + H_2O \tag{13}$$

As shown in Fig. 13A, the CO_2^+ signal was much higher than that of H_2O^+, implying that the disproportionation reaction (Eq. (12)) was quite serious. Surprisingly, the process of desulfurization over 50% Mn-Fe/FSM-16 was different from that over pure 50% Mn/FSM-16 sorbent. Fig. 13B showed that the signals at $m/z = 18$ and 44 were much weaker initially when compared with that over 50% Mn/FSM-16, which implied that only a small amount of active constituents
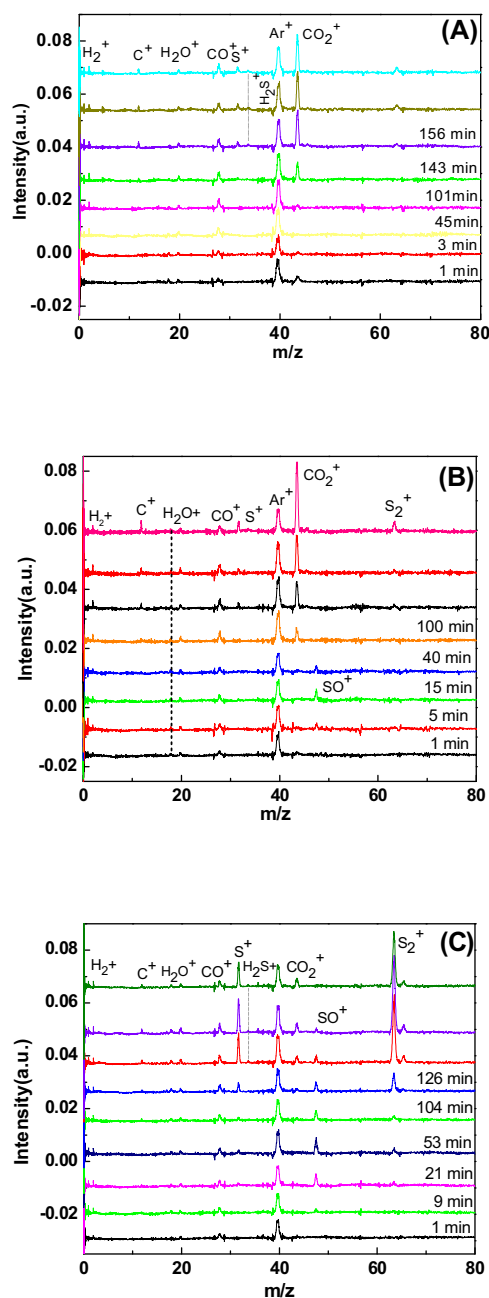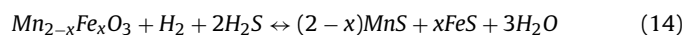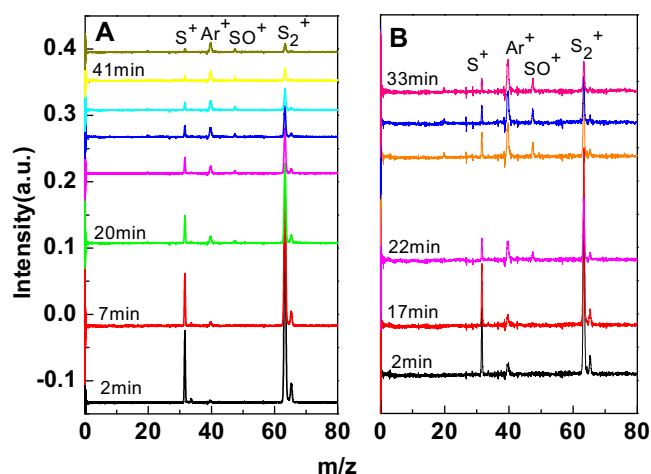
Fig. 14. TOF-MS spectra of regeneration over used (A) 50% Mn/FSM-16 and (B) 50% 4Mn1Fe/FSM-16 at 600 °C using 5% (vol) O_2/Ar mixture under supersonic jet expansion conditions.

of catalytic action of FeS in the heterogeneous thermal decomposition of H_2S: $(1) FeS + H_2S \rightarrow FeS_2 + H_2$; $(2) FeS_2 \rightarrow FeS + 1/2S_2$. Chu et al. [55] reported the formation of CS_2 over Fe_2O_3/SiO$_2$ sorbents using on-line FT-IR technique but we did not observe any CS_2 signal at $m/z = 76$. However, no diffraction peak of elemental sulfur was observed in XRD pattern of the used sorbent (Fig. 2), which was because the sulfur was existed in amorphous form or already sublimed. As for the Mo doped Mn-Fe sorbent (Fig. 13C), it exhibited similar H_2S removal process to 50% Mn-Fe/FSM-16. Due to the incorporation of Mo species, which restrained the reduction of 50% 4Mn1Fe-3%Mo/FSM-16, it was difficult to find any signal of the reduction products at the initial stage. However, an intensive SO$^+$ signal was observed after the sorbent was exposed to H_2S for 9 min. This was attributed to the interactions between Fe and Mo species, mainly in dispersion and electronic effects or the strong oxidation ability of Mo^{6+}. Mo species promoted the dispersion of particles and provided more surface atoms or more active sites, which led to more H_2S being oxidized. Zhang et al. [37] reported recently that Mo interacted with Fe species *via* the Fe-O-Mo bridge structure and charge transfer caused an electron-deficient state of Fe species. Therefore, H_2S was oxidized more easily under such circumstances. Due to the cooperative catalytic activity of FeS and MoS$_2$, stronger signal of S_2^+ was observed, which could be an important reason for the increase in sulfur capacity. It is interesting to note that the intensity of CO_2^+ and C$^+$ peaks were much weaker compared to 50% 4Mn1Fe/FSM-16 and 50% Mn/FSM-16 sorbents, which verified that the Mo modified Mn-based sorbents could effectively lower the carbon deposition. This was considered to be a favorable condition for assuring stable activity during desulfurization. This phenomenon was ascribed to a large amount of CO_2 adsorption on surface of MoS$_2$, which could not be released in time to enter into the gas phase and suppressing the occurrence of disproportionation reaction [56].

After sulfurization, 5 vol% O_2/Ar mixture was released into the reactor for regeneration over the used 50% Mn/FSM-16 (29 mg) and 50% 4Mn1Fe/FSM-16 (15 mg). TOF-MS spectra of the regenerated sorbents were shown in Fig. 14. It could be seen that there was a similar TOF-MS signal to be observed over different sorbents. Besides the signal of the carrier gas Ar$^+$ ($m/z = 39$), two peaks at $m/z = 32$ and 64 were observed at the initial stage, which could originate from O_2^+, S$^+$, SO$_2^+$ or S_2^+. In order to further distinguish them, the used 50% 4Mn1Fe-3%Mo/FSM-16 (12 mg) was regenerated at the atmosphere of 6 vol% $^{18}O_2$/Ar mixture (Fig. 15). It was observed that before the regeneration, the thermal desorp-
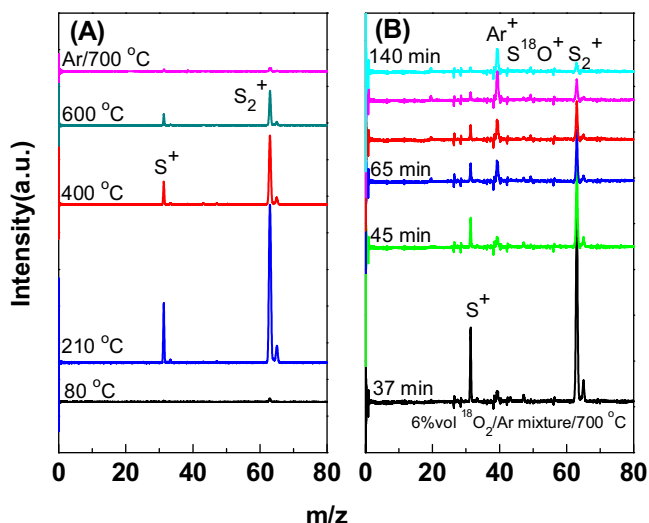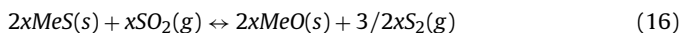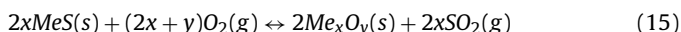

Fig. 13. TOF-MS spectra of products over (A) 50% Mn/FSM-16, (B) 50% 4Mn1Fe/FSM-16 and (C) 50% 4Mn1Fe-3% Mo/FSM-16 at 600 °C under supersonic jet expansion conditions (1.5% H_2S, 10.5% H_2, 18% CO, and Ar balance).

in the sorbent were reduced, this was consistent with the result obtained from TPR. The following equation shows the reaction:

$$Mn_{2-x}Fe_xO_3 + H_2 + 2H_2S \leftrightarrow (2-x)MnS + xFeS + 3H_2O \quad (14)$$

However, the presence of a new weak peak at $m/z = 48$, which was assigned to the signal of SO$^+$, indicated the formation of a small amount of SO_2 during H_2S removal. Since the oxidation ability of Fe^{3+} is stronger than that of Mn^{3+}, it is concluded that SO_2 can be derived from the oxidation of H_2S by Fe_2O_3. As the sulfidation reaction proceeds, the disappearance of SO$^+$ signal from TOF-MS spectrum was due to the consumption of ferric oxides. With the breakthrough of H_2S, the peak at $m/z = 64$ increased gradually. If the peak at $m/z = 64$ was assigned to SO_2^+, there should be a peak of SO$^+$ at $m/z = 48$ that was from the dissociation of SO_2^+ [54]. Thus, the peak was attributed to S_2^+, whose formation was a consequent

Fig. 15. TOF-MS signals of (A) thermal desorption and (B) regeneration over used 50% 4Mn1Fe-3%Mo/FSM-16 using 6% (vol) $^{18}O_2$/Ar mixture at 700 °C under supersonic jet expansion conditions.

tion signals of S^+ and S_2^+ decreased gradually with an increase in temperature (Fig. 15A), which revealed the existence of abundant elemental sulfur in used 50% 4Mn1Fe-3%Mo/FSM-16 sorbent, similar to the observation in outlet of the reactor at atmospheric condition. After S_2^+ and S^+ signals fully disappeared (Fig. 15A), the pure argon was switched to a mixture of 6 vol% $^{18}O_2$/Ar for the regeneration (Fig. 15B). It could be seen that the strong S^+ and S_2^+ signals persisted, meaning that the formation of elemental sulfur during regeneration (Fig. 15B) because no peaks at m/z = 36 or 68 belonged to $^{18}O_2^+$ or $S^{18}O_2^+$, respectively were observed. Therefore, it could be deduced that the metal sulfides were transformed into metal oxides according to following reactions:

$$2xMeS(s) + (2x + y)O_2(g) \leftrightarrow 2Me_xO_y(s) + 2xSO_2(g) \quad (15)$$

$$2xMeS(s) + xSO_2(g) \leftrightarrow 2xMeO(s) + 3/2xS_2(g) \quad (16)$$

As there generation process continued, the weak peaks at m/z = 48 (Fig. 14B) and 50 (Fig. 15B) that were attributed to SO^+ and $S^{18}O^+$ appeared. This was an indication of a small amount of SO_2 was released at the end of the regeneration reaction. According to earlier reports in the literature, the formation of significant amounts of elemental sulfur occurred only when sorbents were regenerated in $H_2O–O_2$ or SO_2 atmosphere[52,57]. Hence a large number of sulfur presented in diluted oxygen environment meant that the SO_2 produced (Eq. (15)) during regeneration could react rapidly with sulfide nanoparticles (Eq. (16)). As a result, all SO_2 were converted to elemental sulfur before the end of regeneration, which was condensed at the exit of the sorbent bed. When the regeneration reaction was coming to an end, the signal intensity of the elemental sulfur decreased gradually and weak signal of SO_2 appeared due to the exhaustion of metal sulfides. Besides, based on TOF-MS spectrum analysis, the temperature could not affect very much the generation products.

4. Conclusion

A cost-effective mesoporous 50% 4Mn1Fe-3%Mo/FSM-16 sorbent was synthesized and its desulfurization performance was evaluated at 600 °C in hot coal gas. The highest BSC (18.15 g S/100 g sorbent) was obtained on this sorbent due to high dispersion of nanoparticles. After sulfurization, the used sorbent could be regenerated completely in a simple way, which verified that it was renewable and durable. Elemental sulfur was produced instead of SO_2 during regeneration, which avoided the process for further treatment of SO_2. In addition, the mechanism of sulfidation/regeneration was proposed and studied by highly sensitive TOF-MS technique using $^{18}O_2$ isotope label for the first time. 50% 4Mn1Fe-3%Mo/FSM-16 is a promising sorbent which ensures an efficient and economical process of hot coal gas desulfurization.

References

[1] G. Qi, L. Fu, B.H. Choi, E.P. Giannelis, Energy. Environ. Sci. 5 (2012) 7368–7375.
[2] X. Wang, X. Ma, S. Zhao, B. Wang, C. Song, Energy Environ. Sci. 2 (2009) 878–882.
[3] B. Guo, L. Chang, K. Xie, Ind. Eng. Chem. Res. 53 (2014) 8874–8880.
[4] S.Y. Jung, S.J. Lee, T.J. Lee, C.K. Ryu, J.C. Kim, Catal. Today 111 (2006) 217–222.
[5] Z.F. Zhang, B.S. Liu, F. Wang, J.F. Li, Energy Fuels 27 (2013) 7754–7761.
[6] D. Vamvuka, C. Arvanitidis, D. Zachariadis, Environ. Eng. Sci. 21 (2004) 525–548.
[7] E. Sasaoka, T. Ichio, S. Kasaoka, Energy Fuels 6 (1992) 603–608.
[8] B. Dou, C. Wang, H. Chen, Y. Song, B. Xie, Y. Xu, C. Tan, Chem. Eng. Res. Des. 90 (2012) 1901–1917.
[9] P.R. Westmoreland, D.P. Harrison, Environ. Sci. Technol. 10 (1976) 659–661.
[10] M. Kobayashi, H. Shirai, M. Nunokawa, Energy Fuels 16 (2002) 601–607.
[11] M. Kobayashi, H. Shirai, M. Nunokawa, Ind. Eng. Chem. Res. 39 (2000) 1934–1943.
[12] D. Liu, S. Chen, X. Fei, C. Huang, Y. Zhang, Ind. Eng. Chem. Res. 54 (2015) 3556–3562.
[13] H.L. Fan, T. Sun, Y.P. Zhao, J. Shangguan, J.Y. Lin, Environ. Sci. Technol. 47 (2013) 4859–4865.
[14] B.S. Liu, X.N. Wei, Y.P. Zhan, R.Z. Chang, F. Subhan, C.T. Au, Appl. Catal. B: Environ. 102 (2011) 27–36.
[15] H. Fan, K. Xie, J. Shangguan, F. Shen, C. Li, J. Nat. Gas Chem. 16 (2007) 404–408.
[16] M. Flytzani-Stephanopoulos, M. Sakbodin, Z. Wang, Science 312 (2006) 1508–1510.
[17] J.P. Wakker, A.W. Gerritsen, J.A. Moulijn, Ind. Eng. Chem. Res. 32 (1993) 139–149.
[18] F.M. Zhang, B.S. Liu, Y. Zhang, Y.H. Guo, Z.Y. Wan, F. Subhan, J. Hazard. Mater. 233–234 (2012) 219–227.
[19] T.H. Ko, H. Chu, Y.J. Liou, J. Hazard. Mater. 147 (2007) 334–341.
[20] F. Yin, J. Yu, S. Gupta, S. Wang, D. Wang, J. Dou, Fuel Process. Technol. 117 (2014) 17–22.
[21] Y. Zhang, B.S. Liu, F.M. Zhang, Z.F. Zhang, J. Hazard. Mater. 248–249 (2013) 81–88.
[22] A. Ates, G. Azimi, K.H. Choi, W.H. Green, M.T. Timko, Appl. Catal. B: Environ. 147 (2014) 144–155.
[23] Z.F. Zhang, B.S. Liu, F. Wang, S. Zheng, Chem. Eng. J. 272 (2015) 69–78.
[24] D. Wang, J. Yu, L. Chang, D. Wang, Chem. Eng. J. 166 (2011) 362–367.
[25] Z.B. Huang, B.S. Liu, F. Wang, R. Amin, Appl. Surf. Sci. 353 (2015) 1–10.
[26] M. Mureddu, I. Ferino, E. Rombi, M.G. Cutrufello, P. Deiana, A. Ardu, A. Musinu, G. Piccaluga, C. Cannas, Fuel 102 (2012) 691–700.
[27] H. Xia, F.M. Zhang, Z.F. Zhang, B.S. Liu, Phys. Chem. Chem. Phys. 17 (2015) 20667–20676.
[28] S. Inagaki, A. Koiwai, N. Suzuki, Y. Fukushima, K. Kuroda, Bull. Chem. Soc. Jpn 69 (1996) 1449–1457.
[29] B.S. Liu, Y. Zhang, J.F. Liu, M. Tian, F.M. Zhang, C.T. Au, A.S.-C. Cheung, J. Phys. Chem. C 115 (2011) 16954–16962.
[30] M. Tian, B.S. Liu, M. Hammonds, N. Wang, P.J. Sarre, A.S.-C. Cheung, Phys. Chem. Chem. Phys. 14 (2012) 6603–6610.
[31] T.Q. Zhao, Q. Li, B.S. Liu, R.K.E. Gover, P.J. Sarre, A.S.-C. Cheung, Phys. Chem. Chem. Phys. 18 (2016) 3489–3496.
[32] S. Garg, K. Soni, M. Kumar, T. Bhaskar, J.K. Gupta, K.S.R. Rao, G.M. Dhar, Catal. Today 198 (2012) 263–269.
[33] S. Inagaki, Y. Fukushima, K.J. Kuroda, Chem. Soc. Chem. Commun. (1993) 680–682.
[34] M. Camblor, A. Corma, J.J. Perez-Pariente, Chem. Soc. Chem. Commun. (1993) 557–559.
[35] M.S. Ghattas, Micropor. Mesopor. Mater. 97 (2006) 107–113.
[36] L. Dong, K. Chen, Y. Chen, J. Solid State Chem. 129 (1997) 30–36.
[37] S. Qin, C. Zhang, J. Xu, Y. Yang, H. Xiang, Y. Li, Appl. Catal. A 392 (2011) 118–126.
[38] F. Zhang, Yan, H. Yang, Y.Y. Meng, C. Yu, B. Tu, D. Zhao, J. Phys. Chem. B 109 (2005) 8723–8732.
[39] H. Zhao, D. Zhang, F. Wang, T. Wu, J. Gao, Process Saf. Environ. Prot. 86 (2008) 448–454.

[40] M. Al-Dossary, A.A. Ismail, J.L.G. Fierro, H. Bouzid, S.A. Al-Sayari, Appl. Catal. B: Environ. 165 (2015) 651–660.

[41] S. Yang, F. Qi, S. Xiong, H. Dang, Y. Liao, P.K. Wong, J. Li, Appl. Catal. B: Environ. 181 (2016) 570–580.

[42] X. Tang, J. Li, L. Sun, J. Hao, Appl. Catal. B: Environ. 99 (2010) 156–162.

[43] F. Arena, T. Torre, C. Raimondo, A. Parmaliana, Phys. Chem. Chem. Phys. 3 (2001) 1911–1917.

[44] O.Y. Gutiérrez, D. Valencia, G.A. Fuentes, T. Klimova, J. Catal. 249 (2007) 140–153.

[45] S. Velu, N. Shah, T.M. Jyothi, S. Sivasanker, Micropor. Mesopor. Mater. 33 (1999) 61–75.

[46] M. Baldi, F. Milella, J.M. Gallardo-Amores, J. Mater. Chem. 8 (1998) 2525–2531.

[47] Z.B. Huang, B.S. Liu, X.Y. Tang, X.H. Wang, R. Amin, Fuel 177 (2016) 217–225.

[48] F. Wang, B.S. Liu, Z.F. Zhang, S. Zheng, Ind. Eng. Chem. Res. 54 (2015) 8405–8416.

[49] J. Wang, B. Qiu, L. Han, G. Feng, Y. Hu, L. Chang, W. Bao, J. Hazard. Mater. 213–214 (2012) 184–192.

[50] J. Wang, L. Liu, L. Han, Y. Hu, L. Chang, W. Bao, Fuel Process. Technol. 110 (2013) 235–241.

[51] R. Ben-Slimane, M. Hepworth, Energy Fuels 8 (1994) 1175–1183.

[52] W.J. Bakker, F. Kapteijn, J.A. Moulijn, Chem. Eng. J. 96 (2003) 223–235.

[53] B.S. Liu, Z.Y. Wan, F. Wang, Y.P. Zhan, M. Tian, A.S.C. Cheung, J. Hazard. Mater. 267 (2014) 229–237.

[54] P. Bradt, F.L. Mohler, V.H. Dibeler, J. Res. Nat. Bureau Stand. 57 (1956) 223.

[55] Y.H. Lin, Y.C. Chen, H. Chu, Chemosphere (2015) 62–67.

[56] T. Osaki, T. Horiuchi, K. Suzuki, T. Mori, Appl. Catal. A 155 (1997) 229–238.

[57] J. White, F. Groves, D. Harrison, Catal. Today 40 (1998) 47–57.